Ultrahigh-Efficiency Superior Energy Storage in Lead-Free Films with a Simple Composition

Tianyu Li, Shiqing Deng,* Ruixue Zhu, Jiyuan Yang, Shiqi Xu, Yongqi Dong, Hui Liu, Chuanrui Huo, Peng Gao, Zhenlin Luo, Oswaldo Diéguez, Houbing Huang, Shi Liu, Long-Qing Chen, He Qi,* and Jun Chen*

Read Online

ACCESS | Metrics & More | Article Recommendations | Supporting Information

ABSTRACT: Dielectric capacitors are highly desired in modern electronic devices and power systems to store and recycle electric energy. However, achieving simultaneous high energy density and efficiency remains a challenge. Here, guided by theoretical and phase-field simulations, we are able to achieve a superior comprehensive property of ultrahigh efficiency of 90−94% and high energy density of 85−90 J cm^{-3} remarkably in strontium titanate (SrTiO$_3$), a linear dielectric of a simple chemical composition, by manipulating local symmetry breaking through introducing Ti/O defects. Atomic-scale characterizations confirm that these Ti/O defects lead to local symmetry breaking and local lattice strains, thus leading to the formation of the isolated ultrafine polar nanoclusters with varying sizes from 2 to 8 nm. These nanoclusters account for both considerable dielectric polarization and negligible polarization hysteresis. The present study opens a new realm of designing high-performance dielectric capacitors utilizing a large family of readily available linear dielectrics with very simple chemistry.
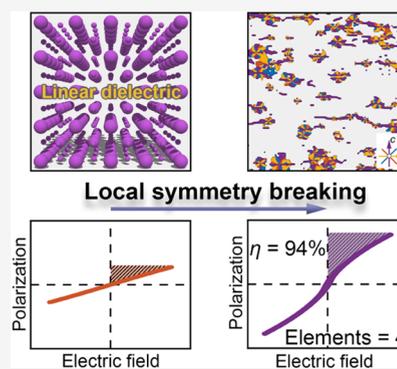
1. INTRODUCTION

Dielectric capacitors, owing to their large power density, high efficiency, and ultrafast charging/discharging rate, have a wide range of applications in modern electronic devices and pulsed power systems and thereby receive extensive attention.[1] Recoverable energy density (U_e) and efficiency (η) are two key parameters that determine the energy-storage performance of the dielectric capacitors. Simultaneous high U_e and high η that constitute the superior energy-storage performance require features including large polarization with a high voltage endurance and low hysteresis (Figure 1a). However, attempts to achieve such a quality of a dielectric capacitor always face challenges due to the intrinsic contradictions among these required features.[2] For example, the dielectrics possessing large polarization tend to have low breakdown strengths (E_b).[3] A typical ferroelectric dielectric can have large polarization but generally exhibits large hysteresis.[4] Thus, the development of a strategy to overcome the low hysteresis, large polarization, and large E_b dilemma would help accelerate progress toward achieving high-performance energy storage.

Over the past two decades, ferroelectrics have been the dominant system of choice for designing high-performance dielectric capacitors because of the large spontaneous polarization and high breakdown strength.[5] Efforts have been mainly focused on overcoming the key challenges to alleviate hysteresis loss (U_{loss}) to reduce energy dissipation and delay its polarization saturation to increase the U_e. The main idea is to break the long-range ordering of the polarization and reduce

the energy barrier during domain switching, which is essentially the origin of hysteresis.[6] Typical strategies include solid solution formation or elemental doping based on lessons learn't from relaxor ferroelectrics, which feature substantially suppressed hysteresis and substantially delayed polarization.[7] The BiFeO$_3$−BaTiO$_3$−SrTiO$_3$ ternary system and Sm-doped BiFeO$_3$−SrTiO$_3$ system are canonical examples among them, wherein the polymorphic nanodomains and the intriguing superparaelectric phase are realized, respectively, both reaching high polarization and low loss simultaneously.[8] Recently, ion bombardment has been confirmed as an effective approach to produce deep-level defect complexes in Pb(Mg,Nb)O$_3$−PbTiO$_3$ relaxor films and to further promote the energy-storage performance.[7c] Such high performance is a result of an elegant combination of a series of components and a delicate balance of different forms of energy. Generally, the appropriate construction of a complex solid solution requires careful compositional design and sophisticated control of the synthesis process. This issue makes the realization of the most attractive energy-storage performance still a quite challenging task.
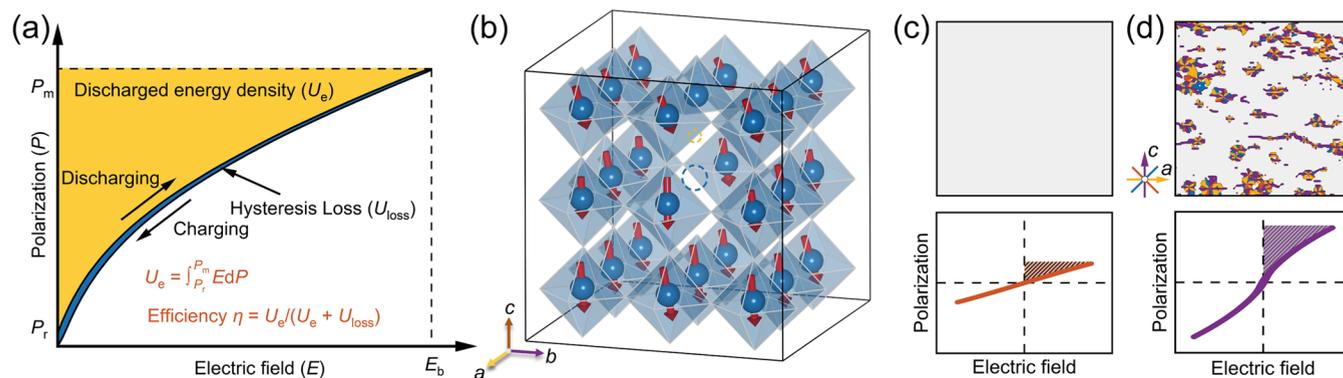
Figure 1. Design of local symmetry breaking in $SrTiO_3$ dielectrics with high-performance capacitive energy storage employing phase-field simulations and ab initio theoretical calculations. (a) Schematic illustration of the energy-storage mechanism in high-performance dielectric materials. (b) First-principles calculation results of a $3 \times 3 \times 3$ Ti/O defect supercell ($V_{Ti}'''' + V_O^{\cdot\cdot}$ configuration with electron doping, see details in Table S1), which reveal local polarization configurations similar to those observed in experiments. The superimposed polar vector denotes the off-centering displacement of the Ti atom relative to the center of TiO_6 octahedra. For clarity, Sr atoms have been omitted, and Ti and O vacancies are marked by dashed blue and yellow circles, respectively. Simulated polar configurations (top) and the corresponding $P-E$ loops (bottom) obtained from phase-field modeling for (c) pure $SrTiO_3$ and (d) local symmetry-broken $SrTiO_3$.

Due to the absence of spontaneous polarization, a large family of centrosymmetric linear dielectrics has been overlooked as candidates for high-performance dielectric capacitors, although most of them are lead-free and environmentally friendly. However, considerable polarization mainly originates from the breaking of spatial inversion symmetry, which can be achieved and effectively tuned by using strategies like strain and defect engineering.[9] We developed a practical methodology for simultaneously realizing high energy-storage performance in a linear dielectric with a simple chemical design by crafting local lattice symmetry breaking to generate substantial localized polarization within an ultrafine region (2−8 nm). The character of the considerable local polarization embedded in the paraelectric matrix well caters to the ideal polarization configuration of a high-performance dielectric capacitor. As a result, we achieved an ultrahigh efficiency and large energy density simultaneously without sacrificing the negligible hysteresis and appreciable E_b nature of linear dielectrics. Using the prototypic linear dielectric $SrTiO_3$ as a model system, we realize an ultrahigh efficiency of 94% with simple chemical compositions (only 4 elements), along with a high energy density of 85 J cm^{-3} that can be comparable with ferroelectric-based capacitors.

2. RESULTS AND DISCUSSION

The first-principles theoretical calculations and phase-field simulations were first conducted to investigate the effect of local symmetry breaking on the dielectric energy-storage performance in the $SrTiO_3$ homoepitaxial film. To introduce local symmetry breaking into the system, we systematically removed a pair of Ti and O atoms from the central unit of a $3 \times 3 \times 3$ supercell. Appropriate electron doping was introduced to maintain the charge neutrality (Figure 1b). It is noted that our theoretical calculations covered a range of defect complexes involving neutral or charged Ti and O vacancies (Table S1). The calculations demonstrate that the defective unit cell is expanded compared to bulk $SrTiO_3$, implying that the nonstoichiometric film would be subjected to an epitaxial compressive strain (Table S1 and Figure S1). Therefore, the Ti/O defect-induced local distortion and substrate strain substantially lower the lattice symmetry and transform from a cubic to a monoclinic-like structure in the vicinal lattices,

where the tensile strains ∼1 and 3% appear along the a and c axis, respectively. This results in large local polarizations (∼55 μC cm^{-2}) based on the Born effective charge approach due to the off-centering movements of cations (∼0.2−0.3 Å) in a low-symmetry structure, which mainly order in [001] directions promoted by the epitaxial strain and show in-plane components as well (polar vectors in Figure 1b and Table S2). To still maintain a highly insulating state for a high breakdown strength, valence-variable transition metals, like manganese, can be further introduced to capture the free charges and increase the energy barrier for the defect migration (see the calculation results in Figure 4d).

The phase-field modeling was conducted to further examine the evolution of the polar configuration and domain structure by modulating the local symmetry. As we expected, the perfect $SrTiO_3$ with a centrosymmetric symmetry forbids the emergence of polar ordering and gives rise to a linear $P-E$ response with tiny polarization upon the electric field loading (Figure 1c). Taking computed results as inputs, randomly positioned a-axis and c-axis lattice strains of about 1 and 3%, respectively, were introduced in the cubic $SrTiO_3$ matrix in our phase-field modeling to break the local symmetry (Figure S2). As a result, polar nanoclusters with sizes less than 10 nm occurred in this local symmetry-broken system (Figure 1d), wherein the polarization angles were found deviating from the [001] direction, as indicated by the theoretical calculations. The emergence of polar nanoclusters in an intrinsic linear dielectric contributes to the prominent spontaneous polarization (25 μC cm^{-2} at ∼2 MV cm^{-1}) and therefore promotes the level of the U_e. A weak interaction between these isolated nanoclusters can avoid the distinct hysteresis arising from the domain-wall motion in the classic ferroelectrics under the external electric field, enabling a high η in the system (Figure 1d).[4] These provide a prerequisite for realizing excellent performance in the $SrTiO_3$ system via local symmetry breaking.

Guided by these theoretical results, we designed and grew a series of $Sr(Ti_{1-x}Mn_x)_{0.88}O_{3-\delta}$ (x_{Mn} = 0, 0.02, 0.04, and 0.08) epitaxial films on (001)-oriented $SrTiO_3$ (STO) or Nb-doped $SrTiO_3$ conductive substrates (Nb:STO) via pulsed laser deposition (the two substrates have the same lattice constant) (Figure S3) (see the Supporting Information for details). The chemical composition of the film was determined by
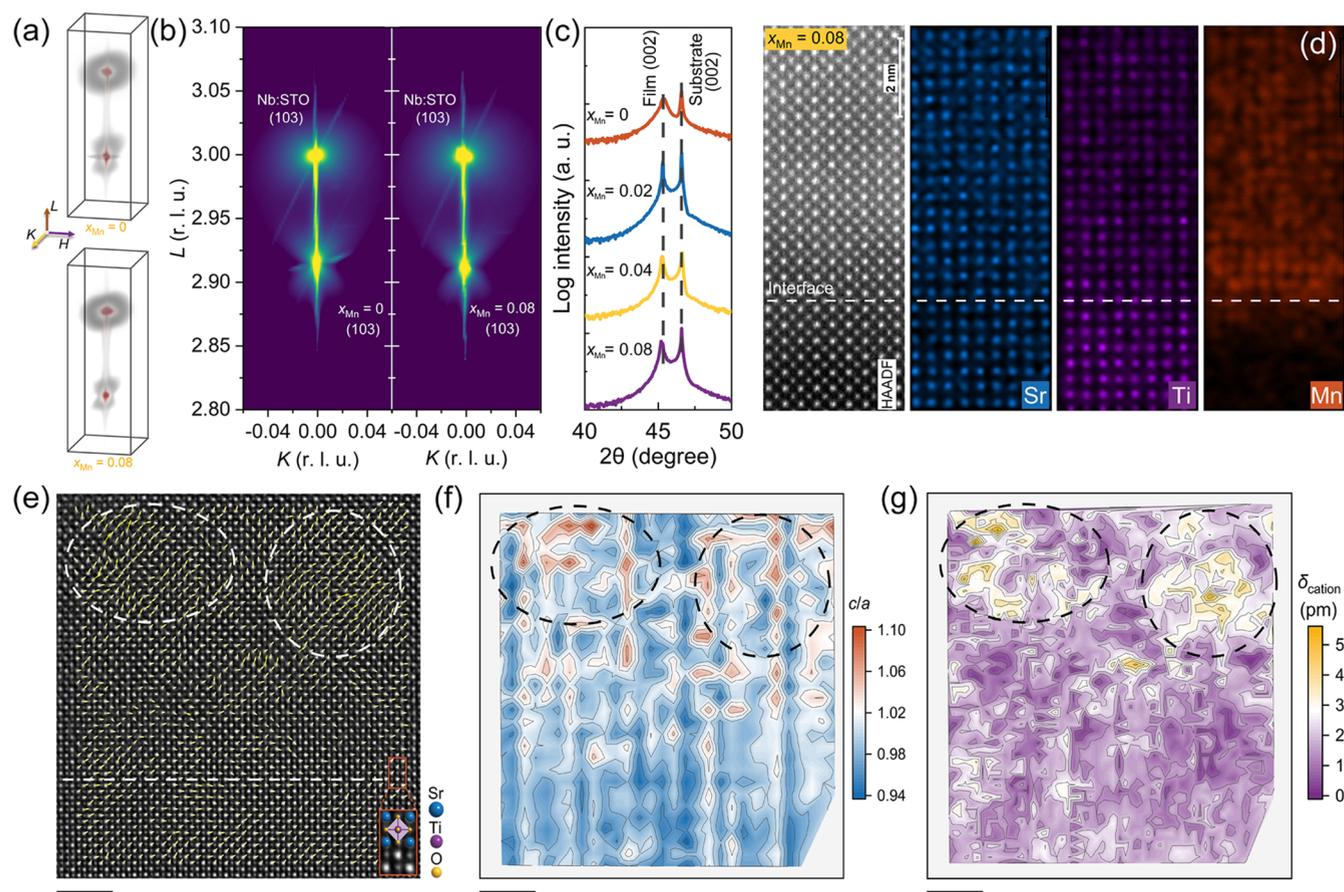
Figure 2. Lattice structure and chemical component characterizations for dielectric thin films. (a, b) Synchrotron-based 3D-RSMs around the (103) Bragg condition and $(1KL)$ cuts for $x_{Mn} = 0$ and 0.08 systems. (c) Out-of-plane XRD patterns for $x_{Mn} = 0$, 0.02, 0.04, and 0.08 films. (d) Atomically resolved energy-dispersive X-ray spectroscopy (EDXS) mappings (Sr, Ti, and Mn elements) of the film−substrate interface for the x_{Mn} = 0.08 film. The image on the left is the corresponding HAADF-STEM image. (e) Integrated differential phase contrast (iDPC)-STEM image of the film−substrate interface for the x_{Mn} = 0.08 film at the [100] zone axis, where the overlaid polar vectors indicate the off-centering movement of Sr and Ti atoms. (f) Maps of unit cell-level c/a ratios and (g) polar vector magnitudes of the region in panel (e), where the polar nanoclusters with local symmetry breaking are circled. The scale bars in panels (e−g) are 2 nm.

inductively coupled plasma mass spectrometry and X-ray photoelectron spectroscopy (XPS) depth profiling tests, which is close to the ceramic target used (Figure S4, Tables S3 and S4). We confirmed the high crystallization quality and favorable epitaxial growth of the films without a detectable secondary phase by atomic force microscopy, low-magnification high-angle annular dark-field scanning transmission electron microscopy (HAADF-STEM) images, and wide-range synchrotron-based X-ray diffraction (SXRD) (Figures S5−S8). The thicknesses of the films range from ∼50 to 500 nm. Synchrotron-based three-dimensional reciprocal space maps (3D-RSMs) around the (103) diffraction conditions and phi-scans of the thin film and substrate (Figures 2a, S9, and S10) indicate a macro tetragonal structure of thin films with an increased c/a ratio of ∼1.03 for all components compared with the cubic substrate ($c/a = 1$). This observation is in line with the splitting of the diffraction spots in the selected area electron diffraction pattern that consists of the thin film and substrate (Figure S11). Such a large c/a ratio in a perovskite oxide provides a foundation for the emergence of a comparable spontaneous polarization resembling that of the prototype ferroelectrics such as $PbTiO_3$ ($c/a = 1.064$ and $P_s = 75 \ \mu C \ cm^{-2}$).[10] The intensity contributions from diffuse scattering near the (103) Bragg condition in the 3D-RSM were

detected for all systems, as shown in Figure 2b. Intriguingly, a butterfly-shaped diffuse-scattering distribution is present for all thin films with diffuse rods canted to $[0\bar{1}1]$ and [011] directions in $(1KL)$ cuts. This feature is commonly observed in relaxor ferroelectrics with polar nanoregions,[11] suggesting local disorders of local polarizations within the thin film. The analysis of the stereoscopic profile of the (103) spot of the film in the 3D-RSM indicates that the diffuse rod lies on a conical surface, with an inclination angle (α) of approximately 30° relative to the <001> direction. This value of α is consistent with our theoretical calculations, where the average value of α is approximately 32° (Table S2). In this regard, a characteristic size of emergent polar clusters can be determined at about 6.1 nm by fitting the diffusing rod profiles.[12] The (103) spot of the thin film is also elongated along the L direction. This suggests a continuous distribution of the lattice constant c or the c/a ratio, corresponding to an inhomogeneous strain inside the films. It is noted that there is a slight enhancement in the c/a ratio, transitioning from 1.028 in the $x_{Mn} = 0$ film to 1.031 in the $x_{Mn} = 0.08$ film (Figure 2c). Besides, the sample with the chemical composition of $Sr(Ti_{0.9},Mn_{0.1})O_3$ ((Ti,Mn)/Sr = 1) was also prepared, which features a negligible lattice distortion ($c/a = 1.003$) in the XRD pattern (Figure S12a). These observations further confirm that local symmetry breaking
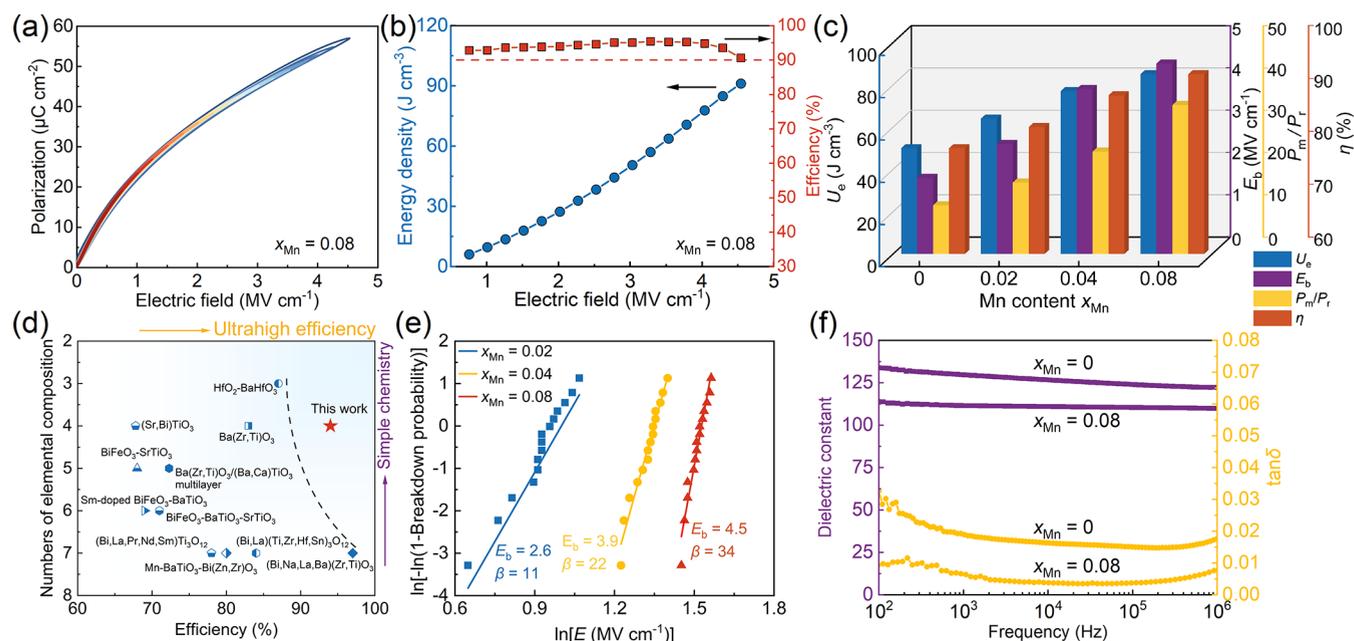
Figure 3. Energy-storage performances of the STO-based dielectric films. (a) Unipolar $P-E$ loops for the $x_{Mn} = 0.08$ film with a thickness of 394 nm. (b) Energy density and efficiency of the $x_{Mn} = 0.08$ film as a function of the external electric field, derived from unipolar $P-E$ loops. (c) U_e, η, P_m/P_r, and E_b values with respect to the Mn content x_{Mn}. (d) Comparison of the efficiency and number of elemental components of the $x_{Mn} = 0.08$ system under E_{max} with the representative high-performance lead-free ferroelectric film capacitors.[7a,8a,b,19] (e) Statistical breakdown strengths of systems fitted by the Weibull distribution. The slope parameter β describes the discreteness of E_b data. (f) Frequency-dependent dielectric constant and loss tangent ($\tan\delta$) for $x_{Mn} = 0$ and 0.08 films.

mainly arises from nonstoichiometry-induced Ti/O defect complexes.

To obtain atomic-scale insights into the local structure and polar configuration, state-of-the-art aberration-corrected STEM imaging technology was utilized. Figures 2d and S13 show the atomically resolved energy-dispersive X-ray spectroscopy (EDXS) maps of the local element distribution near the substrate−film interface. In contrast to the almost unchanged Sr contents from the substrate to the thin film, the Ti elements show an obvious deficiency in the film part. Meanwhile, the substituted Mn atoms are found uniformly distributed in the film. The simultaneously acquired HAADF-STEM image, as well as the low-magnification image (Figures S6 and S7), manifests an unbroken perovskite structure of the film showing the absence of other defects, like interfacial dislocation or Ruddlesden−Popper stacking faults.[13] Intriguingly, many contrast-blurred nanoclusters emerge in the close-up annular bright-field image, which features a decreased intensity of Ti/O atomic columns and a clear lattice distortion (Figure S14). This observation is consistent with the fact that only point defects of Ti/O vacancies should exist in the films and subsequently provoke local symmetry breaking, in good accordance with the theoretical calculations. Integrated differential phase contrast (iDPC) imaging was performed to characterize the nature of the local symmetry, where both the heavy and light elements are visible simultaneously.[14] Figure 2e shows an iDPC-STEM image near the film−substrate interface for the $x_{Mn} = 0.08$ film. By extracting the precise atom position in the image, we calculated and mapped the polarization displacement (the arrows in Figure 2e denote polar vectors) and the c/a (Figure 2f) unit cell-by-unit cell. Newly observed nanoclusters with increased c/a ratios are observed (marked by dashed black circles, as shown in Figure 2f), manifesting abnormal tetragonal distortion. As expected, such lattice-

distorted nanoclusters feature a local polar ordering with a size of about 2−8 nm, indicated by polar vectors within white circles, as shown in Figure 2e. Averaging the c/a ratios from the entire region of the thin film in the STEM images results in a value of 1.029, which aligns with the results obtained from the SXRD patterns. It is noted that, rather than being well aligned along the [001] direction, the polar vectors within the nanoclusters show evident in-plane components, suggesting a lower local symmetry of a monoclinic-like phase than a perfect tetragonal phase.[15] This character is consistent with the unique diffuse-scattering feature observed in the 3D-RSM. The distribution of polar displacement magnitudes shows that the off-centering cation displacements can reach as high as 20−60 pm inside the nanoclusters (Figure 2g) and we can estimate a considerable spontaneous polarization (P_s) of about 50 μC cm^{-2}. Such a value is comparable to that of classic ferroelectrics, such as tetragonal-like BiFeO$_3$ (~60 μC cm^{-2}) and PbTiO$_3$ (~75 μC cm^{-2}).[10,16] Moreover, such randomly distributed polar nanoclusters also exist in the Mn-absent film ($x_{Mn} = 0$), once again confirming the origin of local symmetry breaking and local polarization in the Ti/O defect rather than Mn substitution (Figure S15). On the basis of these results, one can reasonably deduce that Ti/O defect unit cells are the origins that cause the local lattice strain on the adjacent lattices, break the local symmetry, and drive cations out of their centrosymmetric sites. So far, we have essentially realized a special polarization fashion with highly polar nanoclusters embedded in a nonpolar matrix, being analogous to some classic relaxor ferroelectrics and implying an attractive energy-storage performance.[17]

The energy-storage performances of the systems were then characterized by measuring electric field-dependent polarization ($P-E$) loops. $P-E$ loops of the thin films with different Mn contents all feature an extremely slim shape and small
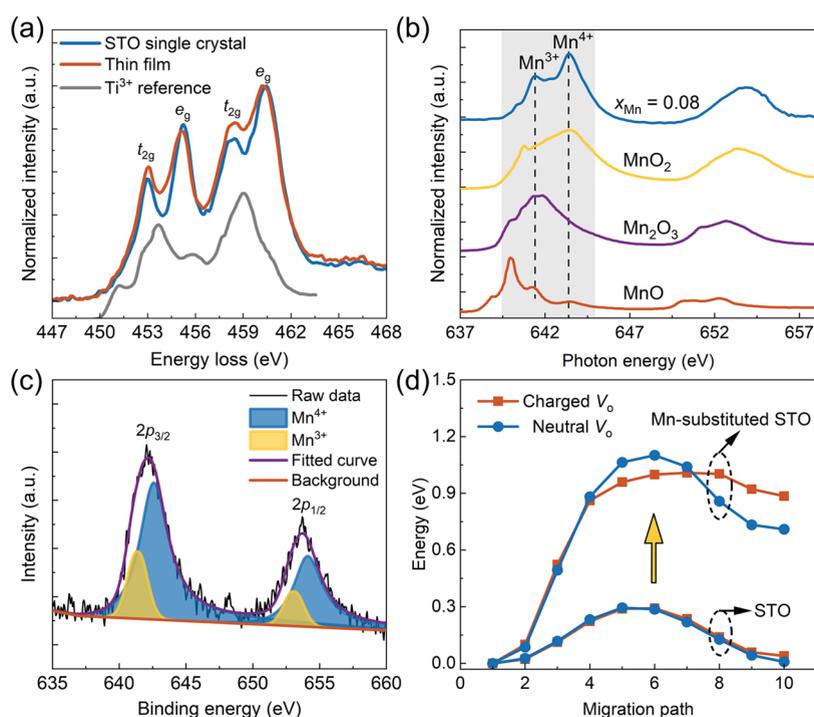
Figure 4. Electronic investigations and density functional theory (DFT) calculations on the origin of high energy-storage performance. (a) Ti $L_{2,3}$-edge EELS spectra of the thin film, single-crystal substrate, and Ti^{3+} spectra.[22] (b) Mn $L_{2,3}$-edge XAS spectra compared with MnO, Mn_2O_3, and MnO_2 spectra.[24] (c) Mn 2p XPS spectra and fitting curves for the $x_{Mn} = 0.08$ system. (d) Migration energy landscapes of oxygen vacancies for STO and Mn-substituted STO systems based on DFT calculations.

hysteresis (Figures 3a and S16). As the electric field increases, the efficiency maintains a constant of about 94−97% for the $x_{Mn} = 0.08$ film derived from unipolar $P–E$ loops (Figure 3a,b) and sustains over 90% with a large U_e of 90 J cm^{-3} even approaching E_b. When comparing the performance of systems with different Mn contents, one can find that the P_m/P_r ratio of the thin films substantially increases from $x_{Mn} = 0$ to 0.08 with a smaller hysteresis (Figures 3c and S16). This observation predicts good energy-storage performance and highlights the role of Mn doping in enhancing voltage endurance as well as suppressing conductive behavior. The maximum U_e and η reach as high as 85 J cm^{-3} and 94% in the $x = 0.08$ system, respectively, under an external electric field of 4.3 MV cm^{-1}. In general, a large energy density but low efficiency will cause severe energy dissipation and the concomitant thermal effect, seriously shrinking the service life of the material and even incurring thermal breakdown during the charging and discharging cycles.[18] Based on this consideration, η can be an important limiting factor in practical applications, especially for systems with a high energy density. We compared η and numbers of the elemental composition of the $x_{Mn} = 0.08$ sample with the representative lead-free (anti)ferroelectric-based relaxor films (Figure 3d).[7a,8a,b,19] It can be noted that the ultrahigh efficiency of 94%, large energy density of 85 J cm^{-3}, and simple composition of only four elements of the $x_{Mn} = 0.08$ film make it a prominent position, validating the concept of local symmetry breaking and our results from the phase-field simulation and theoretical calculations. The high energy density of 85−90 J cm^{-3} can also be comparable with them. More importantly, a simple composition of the films (only 4 elements) effectively simplifies the chemical design of high-performance dielectric capacitors, which can avoid challenges in the production process induced by strict control of the

complex chemical composition or fine fabrication of the multilayer and superlattice (Figure 3d). Besides, as the (Ti + Mn)/Sr ratio decreases, the increment in hysteresis arising from the higher density of Ti/O defects and larger c/a ratio sharply deteriorates the efficiency although the polarization increases (Figure S3). The chosen Ti + Mn/Sr = 0.88 fraction represents the optimal balance among the energy-storage density, efficiency, and endurance, leading to the best overall energy-storage performance. We further examined the stability of the U_e and η by measuring the $P–E$ loop as functions of temperature, frequency, and charging/discharging cycles. The U_e and η of $x_{Mn} = 0.08$ systems show good stability (vibration <5%) in a wide temperature range of 78−383 K, frequency range of 25 Hz to 1 kHz, thickness range of ∼187−393 nm, and 10^6 cycles (Figures S17 and S18). These features make this system highly promising for practical power-storage applications.

Large voltage endurance and stable dielectric properties also play pivotal roles in improving the energy-storage performance. The Weibull distribution was taken to determine the statistical E_b of the thin films with different x_{Mn} (Figure 3e). From $x_{Mn} = 0.02$ to 0.08, an increase in the Mn content substantially promotes the E_b from 2.6 to 4.5 MV cm^{-1}, exhibiting a high voltage endurance for $x_{Mn} = 0.08$ systems. Further increasing the Mn content (from $x_{Mn} = 0.08$ to 0.20) leads to the deterioration of the voltage endurance performance (Figure S19). This is because excessive Mn atoms act as an acceptor dopant, replacing Ti^{4+} and creating additional oxygen vacancies.[20] This underscores the optimal Mn content of $x_{Mn} = 0.08$. To further probe the dielectric properties and insulating state, we measured the dielectric constant and loss tangent $(\tan\delta)$ as functions of frequency and temperature (Figure 3f). Upon Mn substitution, the dielectric loss decreases

sharply from 0.015 to 0.019 for x_{Mn} = 0 to 0.004−0.006 for x_{Mn} = 0.08 at 10^3−10^5 Hz. The tan δ value of x_{Mn} = 0.08 is located at a very low level in dielectric film capacitors, which avoids thermal dissipation and guarantees a large E_b, high efficiency, and longevity.[1b21] For all components, the dielectric constant and loss show good stability, spanning a wide frequency range from 100 Hz to 1 MHz. Besides, the temperature-dependent dielectric spectrum from 125 to 723 K for x_{Mn} = 0.08 exhibits a typical relaxation behavior, being consistent with the fact of localized polar nanoclusters in the thin film (Figure S20).

To unveil the underlying mechanism of high performance and in particular to build its connection with local symmetry breaking, multiple characterizations of the electronic structure and valence state were performed by using the soft X-ray absorption spectrum (XAS) and the electron energy-loss spectrum (EELS) and were combined with in-depth theoretical assessments. Distinct differences in the Ti $L_{2,3}$-edge EELS spectra of the STO single crystal, the x_{Mn} = 0.08 thin film, and the Ti^{3+} reference[22] can be observed (Figure 4a), suggestive of a substantially changed coordination environment of the Ti atom in the film. The 3d orbital of Ti atoms will degenerate into lower-lying e_g and higher-lying t_{2g} orbitals at TiO$_6$ octahedra and the hybridization states between O 2p and Ti 3d orbitals are highly sensitive to the octahedra distortion and polar displacement of the Ti atom.[23] Ti atoms moving off-center in a low symmetry, such as in a monoclinic-like structure, should give rise to a canting polarization deviated from the [001] to [111] direction. According to crystal-field theory, the t_{2g}-2p hybridization strength would thus be highly reinforced owing to their π interaction. Therefore, the increased intensity of t_{2g} peaks suggests more empty states and resultant strengthened hybridizations in t_{2g}-2p interactions as against the cubic SrTiO$_3$ substrate due to the monoclinic-like polar configuration in strongly distorted TiO$_6$ octahedra. A similar change can also be observed in the Ti $L_{2,3}$-edge XAS spectra (Figure S21). The broadening e_g peak with an asymmetric shape indicates an extra contribution on the low-energy side, resulting from the further degeneracy breaking of the e_g orbital that is associated with the emerged polarization introduced by the Ti off-centering movement. Essentially, such changes in the electronic structure of the thin film have their origin in the Ti/O deficiency, which triggers the emergence of local polarization following our original design intention.

Figure 4b compares the Mn $L_{2,3}$-edge XAS spectra of x_{Mn} = 0.08 with those of the reference samples (MnO, Mn$_2$O$_3$, and MnO$_2$ powders),[24] indicative of a mixed-valence state of Mn^{3+} and Mn^{4+} in the film, which is in accord with the XPS results, as shown in Figure 4c. The ratio between Mn^{3+} and Mn^{4+} is estimated as around 1:2 in the x_{Mn} = 0.08 films by fitting the XPS spectrum. XPS depth profiling was also conducted throughout the thin film, wherein the nearly identical peak profiles eliminated potential artifacts resulting from surface effects and corroborated the reliability of the XPS results. In the perovskite oxides, the existence of O vacancies (V_O) generally leads to the generation of Ti^{3+}, which eventually introduces free carriers into the system and forms a breakdown path under the external electric fields.[25] As shown in Ti L-edge XAS and EELS spectra (Figures 4a and S21), no trace of Ti^{3+} is detected because the existence of Ti^{3+} will tend to decrease the intensity of the t_{2g} peak with the 3d^1 configuration, shift the L_2 and L_3 edges toward a lower energy, or broaden both the t_{2g} and e_g peaks on the low-energy side together.[26] This suggests that the generation of Ti^{3+} ions is suppressed by introducing

Mn atoms and can be confirmed by Ti 2p XPS characterizations (Figure S22). Instead, by adjusting its valence state, Mn ions can couple with V_O to form defect dipoles with deep-level energy states that are hard to migrate compared with a single vacancy located near the Fermi level.[27] In this sense, the existence of Mn^{3+} and Mn^{4+} ions, as confirmed by XAS and XPS results, can be beneficial for alleviating the low E_b values caused by purposely constructed Ti/O defects.

Theoretical calculations based on density functional theory support our assertion. Considering all possible migration paths of oxygen vacancies between adjacent subsites, the migration energy landscapes of oxygen vacancies in the 3 × 3 × 3 STO supercell and the Mn-substituted STO supercell were computed and compared, as shown in Figures 4d and S23. Regardless of the neutral or charged vacancy, the migration of oxygen vacancies becomes more difficult with an elevated energy barrier in Mn-substituted STO compared with that of STO. We found that the breaking of the periodic potential field would make the migration in Mn-substituted STO much more thermodynamically unfavorable, as the energy is greatly increased when oxygen vacancies move from the position of the low-energy state to a nearby position. As a result, the sluggish oxygen vacancy with suppressed mobility by Mn substitution accounts for the low dielectric loss and large slope parameter β that represents a narrow distribution of the E_b at the Weibull tests. Consequently, the breakdown strength is enhanced, and the dielectric properties are also improved in Mn-substituted systems. These results highlight the critical role of transition metals in dielectric capacitors and suggest that the cooperation of different types of defects can reach an optimal state for an improved energy-storage performance.

The attractive energy-storage performance achieved in local symmetry-broken SrTiO$_3$ dielectric films essentially arises from a series of exclusive qualities of the film, including large polarization (57 μC cm^{-2}), low dielectric loss, and negligible hysteresis under high electric fields. Looking back on the design of the material, these qualities are closely correlated to and well reflect different aspects of our construction considerations from different angles. In this regard, the purposely introduced and well-controlled Ti/O vacancies breed localized symmetry breaking and the resulting unique polarization configuration, that is, ultrafine isolated ultrafine polar nanoclusters embedded in a paraelectric matrix, wherein the isolated polar nanoclusters contribute to considerable polarization and meanwhile prevent the hysteresis arising from domain-wall interactions in ferroelectric-based capacitors. Based on our current experimental and theoretical findings, the most reasonable defect state should be the pair of V_{Ti}'''' and $V_O^{\cdot\cdot}$ with electron doping. We also acknowledge that other potential forms of Ti/O defects, such as the individual Ti or O vacancy, cannot be definitively ruled out based on the limitations of the available characterization methods. Further introduction of Mn substitution effectively impedes the migration of these constructed vacancies by increasing their migration energy barriers and captures the additional free charges, which avoids the leakage of the defect-engineered systems in general and thus leads to high breakdown strength (Figure S12). By taking full advantage of local symmetry breaking-accompanied effects and the cooperation of different kinds of defects in linear dielectrics, this simple design idea significantly simplifies the composition and construction process of high-performance energy-storage capacitors. Furthermore, the attendant excellent performance in environment-

friendly STO systems taking rise in the advantages of both ultrahigh efficiency (η = 94%) and high energy density (U_e = 85 J cm^{-3}) makes the system an up-and-coming candidate for high-performance dielectric capacitors. On this basis, starting with a model system, we fully release the tremendous potential of linear dielectrics and open a different realm in the design of capacitive dielectric materials.

3. CONCLUSIONS

Our strategy based on local symmetry breaking allows for high-performance dielectric energy storage in paradigmatic linear dielectric SrTiO$_3$-based thin films. This simple regulating strategy, along with lead-free constituents, avoids intricate compositional or structural design and environmental toxicity. If our strategy works with other linear dielectric systems, this opens up a wide compositional space with materials that have other attractive material properties represented by numerous candidates and environmental friendliness. Beyond dielectric energy storage, our approach also provides an avenue for performance optimization in abundant symmetry-sensitive functionalities such as piezoelectricity and electrostrictive properties, along with navigating the discovery of emergent physical properties triggered by lattice symmetry breaking.

■ ASSOCIATED CONTENT

ⓈI Supporting Information

The Supporting Information is available free of charge at https://pubs.acs.org/doi/10.1021/jacs.3c08903.

> Experimental procedures for phase-field simulations, first-principles theoretical calculations, target and film fabrications, structural characterizations, electric measurements, chemical valence, composition, and electronic structure analyses; details about defect configuration and structural evolution; and details about chemical design (PDF)

■ AUTHOR INFORMATION

Corresponding Authors

Shiqing Deng − Department of Physical Chemistry and Beijing Advanced Innovation Center for Materials Genome Engineering, University of Science and Technology Beijing, Beijing 100083, China; ⓞ orcid.org/0000-0001-7016-4084; Email: sqdeng@ustb.edu.cn

He Qi − Department of Physical Chemistry and Beijing Advanced Innovation Center for Materials Genome Engineering, University of Science and Technology Beijing, Beijing 100083, China; Email: qiheustb@ustb.edu.cn

Jun Chen − Department of Physical Chemistry and Beijing Advanced Innovation Center for Materials Genome Engineering, University of Science and Technology Beijing, Beijing 100083, China; Hainan University, Haikou 570228, China; ⓞ orcid.org/0000-0002-7330-8976; Email: junchen@ustb.edu.cn

Authors

Tianyu Li − Department of Physical Chemistry and Beijing Advanced Innovation Center for Materials Genome Engineering, University of Science and Technology Beijing, Beijing 100083, China; ⓞ orcid.org/0000-0001-8857-433X

Ruixue Zhu − Electron Microscopy Laboratory, School of Physics, and International Center for Quantum Materials, Peking University, Beijing 100871, China

Jiyuan Yang − Key Laboratory for Quantum Materials of Zhejiang Province, Department of Physics, School of Science, Westlake University, Hangzhou, Zhejiang 310024, China

Shiqi Xu − School of Materials Science and Engineering and Advanced Research Institute of Multidisciplinary Science, Beijing Institute of Technology, Beijing 100081, China

Yongqi Dong − National Synchrotron Radiation Laboratory, University of Science and Technology of China, Hefei 230029, China

Hui Liu − Department of Physical Chemistry and Beijing Advanced Innovation Center for Materials Genome Engineering, University of Science and Technology Beijing, Beijing 100083, China; ⓞ orcid.org/0000-0002-4973-9784

Chuanrui Huo − Department of Physical Chemistry and Beijing Advanced Innovation Center for Materials Genome Engineering, University of Science and Technology Beijing, Beijing 100083, China

Peng Gao − Electron Microscopy Laboratory, School of Physics, and International Center for Quantum Materials, Peking University, Beijing 100871, China; ⓞ orcid.org/0000-0003-0860-5525

Zhenlin Luo − National Synchrotron Radiation Laboratory, University of Science and Technology of China, Hefei 230029, China; ⓞ orcid.org/0000-0002-7196-6537

Oswaldo Diéguez − Department of Materials Science and Engineering and Faculty of Engineering, Tel Aviv University, Tel Aviv 69978, Israel

Houbing Huang − School of Materials Science and Engineering and Advanced Research Institute of Multidisciplinary Science, Beijing Institute of Technology, Beijing 100081, China; ⓞ orcid.org/0000-0002-8006-3495

Shi Liu − Key Laboratory for Quantum Materials of Zhejiang Province, Department of Physics, School of Science, Westlake University, Hangzhou, Zhejiang 310024, China; Institute of Natural Sciences, Westlake Institute for Advanced Study, Hangzhou, Zhejiang 310024, China; ⓞ orcid.org/0000-0002-8488-4848

Long-Qing Chen − Department of Materials Science and Engineering, Materials Research Institute, The Pennsylvania State University, University Park, Pennsylvania 16802, United States; ⓞ orcid.org/0000-0003-3359-3781

Complete contact information is available at:
https://pubs.acs.org/10.1021/jacs.3c08903

Notes

The authors declare no competing financial interest.

■ ACKNOWLEDGMENTS

■ REFERENCES

(1) (a) Li, Q.; Chen, L.; Gadinski, M. R.; Zhang, S.; Zhang, G.; Li, H. U.; Iagodkine, E.; Haque, A.; Chen, L.-Q.; Jackson, T. N.; Wang, Q. Flexible high-temperature dielectric materials from polymer nanocomposites. *Nature* **2015**, *523*, 576−579. (b) Palneedi, H.; Peddigari, M.; Hwang, G.-T.; Jeong, D.-Y.; Ryu, J. High-performance dielectric ceramic films for energy storage capacitors: progress and outlook. *Adv. Funct. Mater.* **2018**, *28*, No. 1803665. (c) Wang, G.; Lu, Z.; Li, Y.; Li, L.; Ji, H.; Feteira, A.; Zhou, D.; Wang, D.; Zhang, S.; Reany, I. M. Electroceramics for high-energy density capacitors: status and future perspectives. *Chem. Rev.* **2021**, *121*, 6124−6172.

(2) (a) Herbert, J. M. *Ceramic Dielectrics and Capacitors*; Gordon and Breach: New York, 1985. (b) Prateek; Thakur, V. K.; Gupta, R. K. Recent progress on ferroelectric polymer-based nanocomposites for high energy density capacitors: synthesis, dielectric properties, and future aspects. *Chem. Rev.* **2016**, *116*, 4260−4317.

(3) McPherson, J. W.; Kim, J.; Shanware, A.; Mogul, H.; Rodriguez, J. Trends in the ultimate breakdown strength of high dielectric-constant materials. *IEEE Trans. Electron Devices* **2003**, *50*, 1771−1778.

(4) Damjanovic, D. *The Science of Hysteresis: Hysteresis in Materials*; Bertotti, G.; Mayergoyz, I. D., Eds.; Academic Press: Kidlington, U.K., 2006; Chapter 4, Vol. 3, pp 337−465.

(5) (a) Huang, J.; Scott, J. F. *Ferroelectric Materials for Energy Applications*; John Wiley & Sons, Ltd, 2018. (b) Yang, L.; Kong, X.; Li, F.; Hao, H.; Cheng, Z.; Liu, H.; Li, J.-F.; Zhang, S. Perovskite lead-free dielectrics for energy storage applications. *Prog. Mater. Sci.* **2019**, *102*, 72−108.

(6) (a) Li, F.; Zhang, S.; Damjanovic, D.; Chen, L.-Q.; Shrout, T. R. Local structural heterogeneity and electromechanical responses of ferroelectrics: learning from relaxor ferroelectrics. *Adv. Funct. Mater.* **2018**, *28*, No. 1801504. (b) Yang, L.; Kong, X.; Cheng, Z.; Zhang, S. Ultra-high energy storage performance with mitigated polarization saturation in lead-free relaxors. *J. Mater. Chem. A* **2019**, *7*, 8573−8580.

(7) (a) Cheng, H.; Ouyang, J.; Zhang, Y.-X.; Ascienzo, D.; Li, Y.; Zhao, Y.-Y.; Ren, Y. Demonstration of ultra-high recyclable energy densities in domain-engineered ferroelectric films. *Nat. Commun.* **2017**, *8*, No. 1999. (b) Cho, S.; Yun, C.; Kim, Y. S.; Wang, H.; Jian, J.; Zhang, W.; Huang, J.; Wang, X.; Wang, H.; MacManus-Driscoll, J. L. Strongly enhanced dielectric and energy storage properties in lead-free perovskite titanate thin films by alloying. *Nano Energy* **2018**, *45*, 398−406. (c) Kim, J.; Saremi, S.; Acharya, M.; Velarde, G.; Parsonnet, E.; Donahue, P.; Qualls, A.; Garcia, D.; Martin, L. W. Ultrahigh capacitive energy density in ion-bombarded relaxor ferroelectric films. *Science* **2020**, *369*, 81−84.

(8) (a) Pan, H.; Li, F.; Liu, Y.; Zhang, Q.; Wang, M.; Lan, S.; Zhang, Y.; Ma, J.; Gu, L.; Shen, Y.; Yu, P.; Zhang, S.; Chen, L.-Q.; Lin, Y.-H.; Nan, C.-W. Ultrahigh-energy density lead-free dielectric films via polymorphic nanodomain design. *Science* **2019**, *365*, 578−582. (b) Pan, H.; Lan, S.; Xu, S.; Zhang, Q.; Yao, H.; Liu, Y.; Meng, F.; Guo, E.-J.; Gu, L.; Yi, D.; Wang, X. R.; Huang, H.; MacManus-Driscoll, J. L.; Chen, L.-Q.; Jin, K.-J.; Nan, C.-W.; Lin, Y.-H. Ultrahigh energy storage in superparaelectric relaxor ferroelectrics. *Science* **2021**, *374*, 100−104.

(9) (a) Lee, D.; Lu, H.; Gu, Y.; Choi, S.-Y.; Li, S.-D.; Ryu, S.; Paudel, T. R.; Song, K.; Mikheev, E.; Lee, S.; Stemmer, S.; Tenne, D. A.; Oh, S. H.; Tsymbal, E. Y.; Wu, X.; Chen, L.-Q.; Gruverman, A.; Eom, C. B. Emergence of room-temperature ferroelectricity at reduced dimensions. *Science* **2015**, *349*, 1314−1317. (b) Zhang, L.; Chen, J.; Fan, L.; Diéguez, O.; Wang, J.; Kim, M.; Deng, S.; Wang, J.; Wang,

H.; Deng, J.; Yu, R.; Scott, J. F.; Xing, X.; et al. Giant polarization in super-tetragonal thin films through interphase strain. *Science* **2018**, *361*, 494−497.

(10) Gavrilyachenko, V. G.; Spinko, R. I.; Martynen, M. A.; Fesenko, E. G. Spontaneous polarization and coercive field of lead titanate. *Sov. Phys. Solid State* **1970**, *12*, 1203.

(11) Kim, J.; Takenake, H.; Qi, Y.; Damodaran, A. R.; Fernandez, A.; Gao, R.; MaCarter, M. R.; Saremi, S.; Chung, L.; Rappe, A. M.; Martin, L. W. Epitaxial strain control of relaxor ferroelectric phase evolution. *Adv. Mater.* **2019**, *31*, No. 1901060.

(12) Xu, G.; Shirane, G.; Copley, J. R. D.; Gehring, P. M. Neutron elastic diffuse scattering study of $Pb(Mg_{1/3}Nb_{2/3})O_3$. *Phys. Rev. B* **2004**, *69*, No. 064112.

(13) (a) Lee, C.-H.; Orloff, N. D.; Birol, T.; Zhu, Y.; Goian, V.; Rocas, E.; Haislmaier, R.; Vlahos, E.; Mundy, J. A.; Kourkoutis, L. F.; Nie, Y.; Biegalski, M. D.; Zhang, J.; Bernhagen, M.; Benedek, N. A.; Kim, Y.; Brock, J. D.; Uecker, R.; Xi, X. X.; Gopalan, V.; Nuzhnyy, D.; Kamba, S.; Muller, D. A.; Takeuchi, I.; Booth, J. C.; Fennie, C. J.; Schlom, D. G. Exploiting dimensionality and defect mitigation to create tunable microwave dielectrics. *Nature* **2013**, *502*, 532−536. (b) Kawaguchi, T.; Kawai, T.; Hiraiwa, T.; Sakamoto, N.; Shinozaki, K.; Suzuki, H.; Wakiya, N. Spontaneous superlattice formation and electrical properties of Sr-excess $SrTiO_3$ thin film deposited on $SrTiO_3$ (101) by dynamic aurora pulsed laser deposition. *J. Ceram. Soc. Jpn.* **2021**, *129*, 390−396.

(14) Lazić, I.; Bosch, E. G. T.; Lazar, S. Phase contrast STEM for thin samples: Integrated differential phase contrast. *Ultramicroscopy* **2016**, *160*, 265−280.

(15) Ahart, M.; Somayazulu, M.; Cohen, R. E.; Ganesh, P.; Dera, P.; Mao, H.-K.; Hemley, R. J.; Ren, Y.; Liermann, P.; Wu, Z. Origin of morphotropic phase boundaries in ferroelectrics. *Nature* **2008**, *451*, 545−548.

(16) Wang, J.; Neaton, J. B.; Zheng, H.; Nagarajan, V.; Ogale, S. B.; Liu, B.; Viehland, D.; Vaithyanathan, V.; Schlom, D. G.; Waghmare, U. V.; Spaldin, N. A.; Rabe, K. M.; Wuttig, M.; Ramesh, R. Epitaxial $BiFeO_3$ multiferroic thin film heterostructures. *Science* **2003**, *299*, 1719−1722.

(17) Burns, G.; Dacol, F. H. Glassy polarization behavior in ferroelectric compounds $Pb(Mg_{1/3}Nb_{2/3})O_3$ and $Pb(Zn_{1/3}Nb_{2/3})O_3$. *Solid State Commun.* **1983**, *48*, 853−856.

(18) Li, J.; Shen, Z.; Chen, X.; Yang, S.; Zhou, W.; Wang, M.; Wang, L.; Kou, Q.; Liu, Y.; Li, Q.; Xu, Z.; Chang, Y.; Zhang, S.; Li, F. Grain-orientation-engineered multilayer ceramic capacitors for energy storage applications. *Nat. Mater.* **2020**, *19*, 999−1005.

(19) (a) Peng, B.; Zhang, Q.; Li, X.; Sun, T.; Fan, H.; Ke, S.; Ye, M.; Wang, Y.; Lu, W.; Niu, H.; Scott, J. F.; Zeng, X.; Huang, H. Giant electric energy density in epitaxial lead-free thin films with coexistence of ferroelectrics and antiferroelectrics. *Adv. Electron. Mater.* **2015**, *1*, No. 1500052. (b) Sun, Z.; Ma, C.; Liu, M.; Cui, J.; Lu, L.; Lu, J.; Lou, X.; Jin, L.; Wang, H.; Jia, C.-L. Ultrahigh Energy Storage Performance of Lead-Free Oxide Multilayer Film Capacitors via Interface Engineering. *Adv. Mater.* **2017**, *29*, No. 1604427. (c) Pan, H.; Ma, J.; Ma, J.; Zhang, Q.; Liu, X.; Guan, B.; Gu, L.; Zhang, X.; Zhang, Y.-J.; Li, L.; Shen, Y.; Lin, Y.-H.; Nan, C.-W. Giant Energy Density and High Efficiency Achieved in Bismuth Ferrite-Based Film Capacitors via Domain Engineering. *Nat. Commun.* **2018**, *9*, No. 1813. (d) Luo, J.; Zhu, H.; Zheng, T.; Qiao, H.; Liu, Y.; Lyu, Y. A slush-like polar structure for high energy storage performance in a $Sr_{0.7}Bi_{0.2}TiO_3$ lead-free relaxor ferroelectric thin film. *J. Mater. Chem. A* **2022**, *10*, 7357−7365. (e) Jiang, X.; Lv, J.; Chen, Z.; Shen, Z.; Wang, J.; Deng, Z.; Cao, M.; Yao, Z.; Zhang, S.; Liu, H.; Hao, H. Superior energy storage $BaTiO_3$-based amorphous dielectric film with polymorphic hexagonal and cubic nanostructures. *Chem. Eng. J.* **2022**, *431*, No. 133447. (f) Yang, B.; Zhang, Y.; Pan, H.; Si, W.; Zhang, Q.; Shen, Z.; Yu, Y.; Lan, S.; Meng, F.; Liu, Y.; Liu, Y.; Huang, H.; He, J.; Gu, L.; Zhang, S.; Chen, L.-Q.; Zhu, J.; Nan, C.-W.; Lin, Y.-H. Engineering relaxors by entropy for high energy storage performance. *Nat. Energy* **2022**, *21*, 1074−1080. (g) Yang, B.; Zhang, Q.; Huang, H.; Pan, H.; Zhu, W.; Meng, F.; Lan, S.; Liu, Y.; Wei, B.; Liu, Y.; Yang, L.; Gu, L.; Chen, L.-

Q.; Nan, C.- W.; Lin, Y.-H. Engineering relaxors by entropy for high energy storage performance. *Nat. Energy* **2023**, *8*, 956−964. (h) Yu, Y.; Zhang, Q.; Xu, Z.; Zheng, W.; Xu, J.; Xi, Z.; Zhu, L.; Ding, C.; Cao, Y.; Zheng, C.; Qin, Y.; Li, S.; Li, A.; Wu, D.; Rabe, K. M.; Liu, X.; Wen, Z. Structure-evolution-designed amorphous oxides for dielectric energy storage. *Nat. Commun.* **2023**, *14*, No. 3031.

(20) (a) Hayashi, K.; Ando, A.; Hamaji, Y.; Sakabe, Y. Study of the valence state of manganese ions in $PbTiO_3$ ceramics by means of ESR. *J. Appl. Phys.* **1998**, *37*, 5327−5240. (b) Hejazi, M. M.; Taghaddos, E.; Safari, A. Reduced Leakage current and enhanced ferroelectric properties in Mn-doped $Bi_{0.5}Na_{0.5}TiO_3$-based thin films. *J. Mater. Sci.* **2013**, *48*, 3511−3516. (c) Huang, J.-Z.; Wang, Y.; Lin, Y.; Li, M.; Nan, C.-W. Effect of Mn doping on electric and magnetic properties of $BiFeO_3$ thin films by chemical solution deposition. *J. Appl. Phys.* **2009**, *106*, No. 063911.

(21) Guo, X.; Pu, Y.; Wang, W.; Zhang, L.; Ji, J.; Shi, R.; Shi, Y.; Yang, M.; Li, J. High insulation resistivity and ultralow dielectric loss in La-doped $SrTiO_3$ giant permittivity ceramics through defect chemistry optimization. *ACS Sustainable Chem. Eng.* **2019**, *7*, 13041−13052.

(22) Sefat, A. S.; Amow, G.; Wu, M.-Y.; Botton, G. A.; Greedan, J. E. High-resolution EELS study of the vacancy-doped metal/insulator system, $Nd_{1−x}TiO_3$, $x = 0$ to 0.33. *J. Solid State Chem.* **2005**, *178*, 1008−1016.

(23) (a) Zhu, G.-Z.; Radtke, G.; Botton, G. A. Bonding and structure of a reconstructed (001) surface of $SrTiO_3$ from TEM. *Nature* **2012**, *490*, 384−387. (b) Li, T.; Deng, S.; Liu, H.; Sun, S.; Li, H.; Hu, S.; Liu, S.; Xing, X.; Chen, J. Strong Room-Temperature Ferroelectricity in Strained $SrTiO_3$ Homoepitaxial Film. *Adv. Mater.* **2021**, *33*, No. 2008316.

(24) Qiao, R.; Chin, T.; Harris, S. J.; Yan, S.; Yang, W. Spectroscopic fingerprints of valence and spin states in manganese oxides and fluorides. *Curr. Appl. Phys.* **2013**, *13*, 544−548.

(25) Baiatu, T.; Waser, R.; Härdtl, K.-H. Dc electrical degradation of perovskite-type titanates: III, a model of the mechanism. *J. Am. Ceram. Soc.* **1990**, *73*, 1663−1673.

(26) Susarla, S.; García-Fernández, P.; Ophus, C.; Das, S.; Aguado-Puente, P.; McCarter, M.; Ercius, P.; Martin, L. W.; Ramesh, R.; Junquera, J. Atomic scale crystal field mapping of polar vortices in oxide superlattices. *Nat. Commun.* **2021**, *12*, No. 6273.

(27) (a) Singh, S. K.; Ishiwara, H.; Maruyama, K. Room temperature ferroelectric properties of Mn-substituted $BiFeO_3$ thin films deposited on Pt electrodes using chemical solution deposition. *Appl. Phys. Lett.* **2006**, *88*, No. 262908. (b) Feng, Y.; Wu, J.; Chi, Q.; Li, W.; Yu, Y.; Fei, W. Defects and aliovalent doping engineering in electroceramics. *Chem. Rev.* **2020**, *120*, 1710−1787.